The Relationship between Enzyme Conformational Change, Proton Transfer, and Phosphoryl Transfer in β-Phosphoglucomutase

Angus J. Robertson,[⊥] Alex L. Wilson,[⊥] Matthew J. Burn, Matthew J. Cliff, Paul L. A. Popelier, and Jonathan P. Waltho*

Read Online

ACCESS | Metrics & More | Article Recommendations | Supporting Information

ABSTRACT: Molecular details for the timing and role of proton transfer in phosphoryl transfer reactions are poorly understood. Here, we have combined QM models, experimental NMR measurements, and X-ray structures to establish that the transition of an archetypal phosphoryl transfer enzyme, βPGM, from a very closed near-attack conformation to a fully closed transition state analogue (TSA) conformation triggers both partial proton transfer from the general acid−base residue to the leaving group oxygen and partial dissociation of the transferring phosphoryl group from the leaving group oxygen. Proton transfer continues but is not completed throughout the reaction path of the phosphoryl transfer with the enzyme in the TSA conformation. Moreover, using interacting quantum atoms (IQA) and relative energy gradient (REG) analysis approaches, we observed that the change in the position of the proton and the corresponding increased electrostatic repulsion between the proton and the phosphorus atom provide a stimulus for phosphoryl transfer in tandem with a reduction in the negative charge density on the leaving group oxygen atom. The agreement between solution-phase ^{19}F NMR measurements and equivalent QM models of βPGM_{WT} and βPGM_{D10N} TSA complexes confirms the protonation state of G6P in the two variants, validating the employed QM models. Furthermore, QM model predictions of an AlF_4 distortion in response to the proton position are confirmed using high resolution X-ray crystal structures, not only providing additional validation to the QM models but also further establishing metal fluorides as highly sensitive experimental predictors of active-site charge density distributions.

KEYWORDS: *enzyme catalysis, phosphoryl transfer, proton transfer, transition state analogue, relative energy gradient*
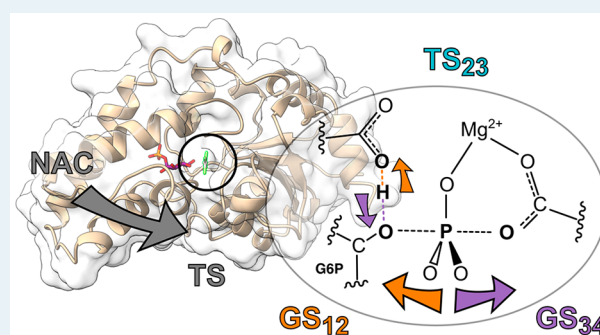
INTRODUCTION

Enzyme-catalyzed transfer of phosphoryl groups is a central process in almost all biological processes in all kingdoms of life.[1] Phosphate monoesters and diesters abound in metabolic pathways and in the storage, maintenance, and expression of genetic information. Correspondingly, the mechanisms employed by phosphoryl transfer enzymes have been the subject of intensive study for many years.[2−6] Phosphate monoesters are labile in the active sites of phosphoryl transfer enzymes but extremely inert in aqueous solutions,[2] and the management of the strong repulsion between phosphate oxygen atoms and the attacking nucleophiles is believed to be a substantial contributor to this behavior.[7] Some phosphoryl transfer enzymes alleviate this repulsion by populating unusual near attack complexes (NACs) in which an attacking nucleophile hydroxyl group hydrogen bonds to phosphate oxygen atoms in a nonproductive orientation.[5,6] The residue that provides general acid−base (GAB) catalysis is proposed not only to modify the electronic properties of the nucleophile (or the leaving group, depending on the direction of the reaction) but also to regulate the alignment of the relevant oxygen atom with the phosphorus atom in an enzyme conformation that supports the transition state (TS) for the chemical step.[4,8] Structural investigations of near TS species have made use of both MgF_3^- and AlF_4^- as transition state analogues (TSAs) that closely mimic the transferring phosphoryl group as they are planar and have a net single negative charge when complexed with substrate in the enzyme active site.[6,9−11] A comparison of NAC and TSA structures supports the hypothesis that the engagement of the GAB residue is concurrent with the phosphoryl group transfer. However, controversy remains as to the timing of proton transfer associated with GAB catalysis, meaning that any detailed interpretation of the mechanism and the energy barrier of the chemical step is open to question.
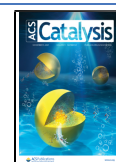
β-Phosphoglucomutase (βPGM) (EC 5.4.2.6) is an archetypal phosphoryl transfer enzyme that utilizes GAB catalysis and has been well-characterized both enzymatically and structurally.[5,10,12−20] It catalyzes the isomerization of β-glucose 1-phosphate (βG1P) and glucose 6-phosphate (G6P) via a β-glucose 1,6-bisphosphate (βG16BP) intermediate. Previous quantum mechanical (QM) models of the phosphoryl transfer between the 1-oxygen of βG16BP and residue D8 of βPGM (to generate G6P) have presented conflicting timings for the proton transfer associated with the GAB residue (residue D10). Analyzing the reaction paths in the direction of phosphoryl group transfer from βG16BP to D8, the predictions in these studies range from "early", through "concerted", and to "late" proton transfer events with calculated barrier heights ranging from 41 to 64 kJ mol^{-1}.[21−24]

The D10N variant of βPGM (βPGM$_{D10N}$) serves as a good model of wild-type βPGM (βPGM$_{WT}$) with the GAB residue in its protonated form.[18] It traps a complex with a novel enzyme conformation, termed here NAC III (Figure 1), in
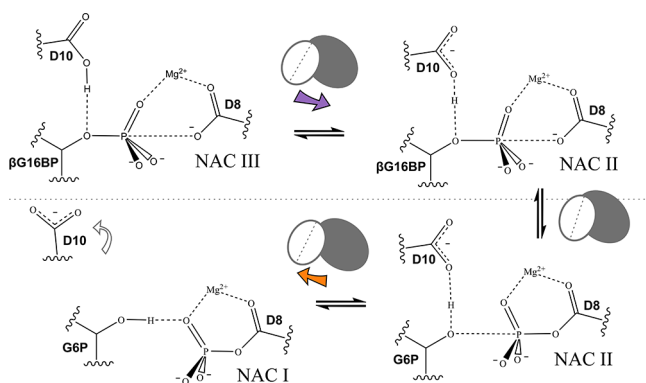
Figure 1. An overview of the relationship between known conformers for closed forms of βPGM and key active-site groups. Schematic representations for (upper left) the reactant complex conformation NAC III,[18] (upper and lower right) the TSA complex conformation NAC II,[17] and (lower left) the product complex conformation NAC I,[5] where the reaction was analyzed in the direction of the phosphoryl group transfer from βG16BP to D8.

which the phosphorus atom of the 1-phosphate group of βG16BP is in van der Waals contact with the nucleophilic carboxylate oxygen of D8; however, the enzyme has not achieved full domain closure. This observation demonstrated that by disfavoring proton transfer from the GAB residue to the bridging oxygen of βG16BP (the leaving group oxygen in this scenario), the phosphate prefers to remain bonded to the sugar and the enzyme does not adopt the conformation that supports the chemical TS. This indicates that a very late proton transfer step is unlikely. However, to determine if the GAB proton is transferred to the nascent sugar hydroxyl group before the peak of the energy barrier during the phosphoryl transfer from βG16BP to D8, experimental validation of QM models of phosphoryl transfer spanning the barrier peak is also required. This is not feasible using native phosphoryl groups but is achievable with a detailed examination of metal fluoride TSA complexes.

Here we have combined QM models, X-ray structures, and NMR measurements to establish that the transition of the βPGM−βG16BP complex from the NAC III to the NAC II or TSA conformation delivers full domain closure, which triggers partial proton transfer from the GAB residue to the leaving

group oxygen. This combination of events also triggers the partial dissociation of the transferring phosphoryl group from the leaving group oxygen. Proton transfer continues but is not completed throughout the reaction path of phosphoryl transfer with the enzyme in the TSA conformation. Moreover, using interacting quantum atoms (IQA) and relative energy gradient (REG) analysis approaches, we observe that the change in the position of the GAB proton and its increased electrostatic repulsion of the phosphorus atom contribute substantially to phosphoryl transfer in tandem with a reduction in the negative charge density on the leaving group oxygen atom. The agreement between solution-phase ^{19}F NMR measurements and equivalent QM models of TSA complexes of βPGM$_{WT}$ and βPGM$_{D10N}$ containing AlF$_4^-$ and G6P confirms that the 1-oxygen of G6P is protonated in the former and deprotonated in the latter. Furthermore, QM model predictions of the AlF$_4$ distortion in response to the positioning of the proton in the hydrogen bond between the 1-oxygen of G6P and the GAB residue were confirmed using a very high-resolution X-ray crystal structure. This not only provides additional validation to the QM models but also further establishes metal fluorides as highly sensitive predictors of active-site charge density distributions.

■ RESULTS

Wild-Type βPGM QM Model. To analyze the chemical step corresponding to conversion of βG16BP to βG6P, a new QM model was constructed for βPGM in its TSA conformation based on the X-ray crystal structure of the wild-type enzyme in its βPGM$_{WT}$−AlF$_4$−G6P complex (PDB 2WF6, 1.4 Å). AlF$_4^-$ moieties are used here rather than MgF$_3^-$ moieties as they are present experimentally in a wider range of βPGM complexes.[6] In such complexes, AlF$_4^-$ replaces the transferring phosphoryl (PO$_3^-$) group and induces the enzyme to enter the fully closed state. In the QM model, the AlF$_4^-$ was substituted with a trigonal planar PO$_3^-$ moiety, and all groups involved in key hydrogen bonding interactions (inclusive of 10 amino acid residues D8, L9, D10, G46, V47, S114, A115, K145, E169, and D170, a Mg^{2+} ion, two water molecules, and βG6P) were included. To guide the fixed boundary positions of this QM$_{WT}$ PO$_3$ model, NMR-derived order parameters (S^2 values) were determined for the backbone amides in the βPGM$_{WT}$−AlF$_4$−G6P complex in solution under conditions reported for its backbone resonance assignment (BioMagRes-Bank (BMRB) 15467).[10] These order parameters measure the degree of local rigidity of backbone amide groups on a subnanosecond time scale. In our model (see the Supporting Information for details), fixed backbone atoms were always ≤2 atoms from a well-ordered ($S^2 \geq 0.8$) amide (Table S1).

The resulting 163 atom QM model (Figure 2) is the largest of this active site studied to date[21−24] and was optimized to a TS using the B3LYP functional[25−28] and standard TS search methods implemented in Gaussian 09,[29] with one negative vibrational mode corresponding to motion of the transferring PO$_3^-$ group along the reaction coordinate. The optimized TS geometry showed only a minor deviation compared to 2WF6, showing that the TSA architecture was retained (Figure 2). Geometries along the reaction coordinate were taken at regular O1$_{G6P}$−P1$_{PO3}$−OD1$_{D8}$ intervals (0.14 Å), and single point energies were evaluated for each of the nine resulting structures. The reaction coordinate was split into four segments (Figure 3), which were defined according to stationary points on the energy profile. Analyzing the reaction
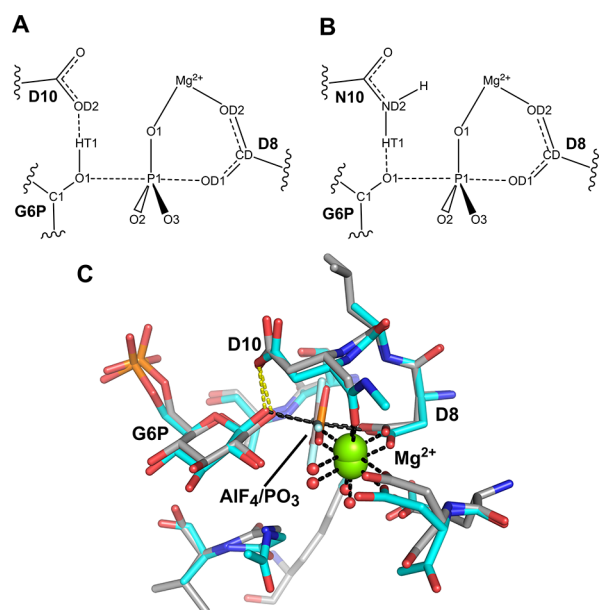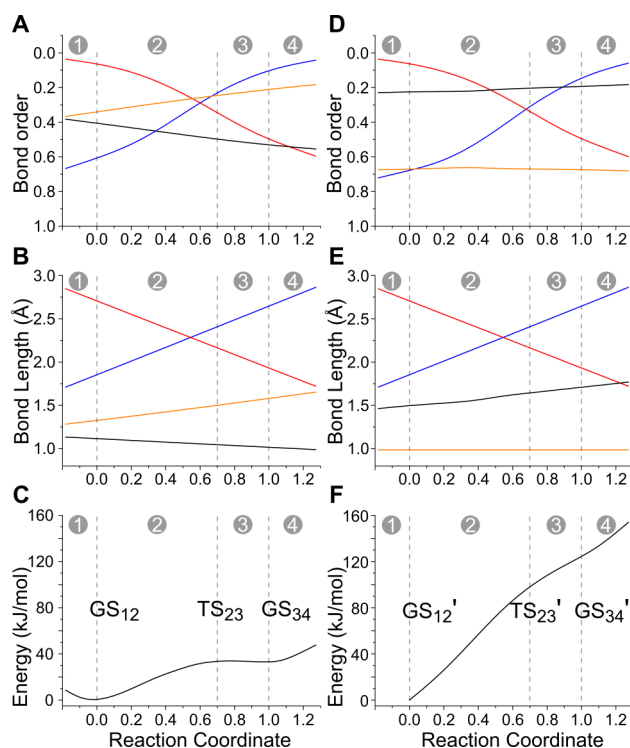
Figure 2. An overview of the βPGM enzyme active site. Schematic representation of key active-site groups in (A) the QM_{WT} PO_3 model and (B) the QM_{D10N} PO_3 model to illustrate the atom labeling used. (C) An annotated cartoon illustration of the 2WF6 βPGM$_{WT}$−AlF$_4$−G6P TSA complex (gray carbon atoms) overlaid with the QM_{WT} PO_3 model of the transition state (cyan carbon atoms). Standard CPK coloring of noncarbon atoms is used, with metal coordination indicated by black dashed lines and selected hydrogen bonds illustrated as yellow dashed lines.

Figure 3. (A−C) QM_{WT} PO_3 and (D−F) QM_{D10N} PO_3 models of phosphoryl transfer, with the reaction coordinate split into four segments. The reaction coordinate is defined according to the calculated positions of GS_{12} and GS_{34} in the QM_{WT} PO_3 model. (A) $P1_{PO3}$−$O1_{G6P}$ (blue line), $P1_{PO3}$−$OD1_{D8}$ (red line), $HT1$−$O1_{G6P}$ (black line), and $HT1$−$OD2_{D10}$ (orange line) bond orders across the reaction path in the QM_{WT} PO_3 model. The bond order y-axis has been inverted for clarity when comparing panel a to panel b and panel d to panel e. (B) $P1_{PO3}$−$O1_{G6P}$ (blue line), $P1_{PO3}$−$OD1_{D8}$ (red line), $HT1$−$O1_{G6P}$ (black line), and $HT1$−$OD2_{D10}$ (orange line) bond lengths across the reaction path in the QM_{WT} PO_3 model. (C) Energy profile across the reaction coordinate in the QM_{WT} PO_3 model. (D) $P1_{PO3}$−$O1_{G6P}$ (blue line), $P1_{PO3}$−$OD1_{D8}$ (red line), $HT1$−$O1_{G6P}$ (black line), and $HT1$−$OD2_{D10}$ (orange line) bond orders across the reaction path in the QM_{D10N} PO_3 model. (E) $P1_{PO3}$−$O1_{G6P}$ (blue line), $P1_{PO3}$−$OD1_{D8}$ (red line), $HT1$−$O1_{G6P}$ (black line), and $HT1$-$OD2_{D10}$ (orange line) bond lengths across the reaction path in the QM_{D10N} PO_3 model. (F) Energy profile across the reaction coordinate in the QM_{D10N} PO_3 model.

path in the direction of phosphoryl transfer from the sugar to the enzyme, i.e., $P1_{PO3}$ moving from $O1_{G6P}$ to $OD1_{D8}$, segment 1 describes the transition from an $O1_{G6P}$−$P1_{PO3}$ distance shorter than the typical O−P bond length (O−P bond lengths are 1.76 Å in the nontransferring distal phosphate group) to what constitutes a ground state (GS_{12}) for the $O1_{G6P}$−$P1_{PO3}$ bond when the protein is in the TSA conformation. Segments 2 and 3 describe the pre- and post-transition state (TS_{23}) transitions, respectively. Segment 4 describes the postformation of the phospho-enzyme ground state (GS_{34}), where the protein is still in the TSA conformation but the $P1_{PO3}$−$OD1_{D8}$ distance is shorter than that in GS_{34}.

An examination of the two ground states associated with the reaction path reveals that in the TSA conformation PO_3^- is already partially dissociated from $O1_{G6P}$ in GS_{12} ($O1_{G6P}$−$P1_{PO3}$ = 1.85 Å) and from $OD1_{D8}$ in GS_{34} ($P1_{PO3}$−$OD1_{D8}$ = 2.00 Å) (Figure 3). It is also apparent that in GS_{12} there is already substantial transfer of the GAB proton (HT1) to the sugar from residue D10 (HT1−$O1_{G6P}$ = 1.12 Å and $OD2_{D10}$−HT1 = 1.33 Å) compared with an average H−O distance of 0.98 ± 0.01 Å of other hydroxyl groups in the model (the protons in the hydrogen bonds are described here using average positions rather than changes in the population between optimal positions linked through QM tunneling). These atom positions illustrate the extent to which proton transfer is linked to the phosphoryl group leaving βG16BP. Additionally, proton transfer is not fully completed by GS_{34} (HT1−$O1_{G6P}$ = 1.03 Å and $OD2_{D10}$−HT1 = 1.56 Å). For comparison, in TS_{23} the HT1−$O1_{G6P}$ distance is 1.04 Å and the $OD2_{D10}$−HT1 distance is 1.51 Å.

To test whether the positioning of atom HT1 (and thus $P1_{PO3}$) in the reaction path was biased according to its starting

position in the structure from which the original QM model was generated (where HT1 was assumed to be bonded to $O1_{G6P}$ in line with previous assumptions about the TSA structure[10]), the TS optimization of the original QM model was repeated four times with the GAB proton starting at different positions spaced between $O1_{G6P}$ and $OD2_{D10}$. The chosen HT1−$O1_{G6P}$ and $OD2_{D10}$−HT1 separations, respectively, were 1.00 and 1.50, 1.20 and 1.30, 1.30 and 1.20, or 1.50 and 1.00 Å. The first three calculations optimized almost exactly to the same TS as was found originally, while the fourth failed to optimize. Hence, displacing the GAB proton toward residue D10 prior to optimization had no significant effect on the position of atoms in the optimized TS structure or the associated reaction path. Overall, our QM_{WT} PO_3 model shows that in the enzyme conformation that supports the chemical TS the GAB proton is preferentially associated with sugar throughout phosphoryl transfer. Therefore, proton transfer can be considered to be early in the reaction path in the direction of phosphoryl transfer from sugar to enzyme, but formally the

proton remains shared throughout the phosphoryl transfer step. The energy barrier from GS_{12} to TS_{23} is +34 kJ mol^{-1}, but in the reverse direction ($GS_{34} \rightarrow TS_{23}$) it is only +1 kJ mol^{-1} (Figure 3). Therefore, despite the modification of the $O1_{G6P}$ leaving group via substantial proton transfer in GS_{12}, the phospho-enzyme state GS_{34} remains considerably destabilized relative to it (+33 kJ mol^{-1}) while the protein is in the TSA conformation.

The equivalent QM model of βPGM_{WT} in its NAC III conformation with $\beta G16BP$ bound was constructed to test whether the substantial transfer of HT1 from $OD2_{D10}$ to $O1_{G6P}$ and the partial dissociation of P1 from $O1_{G6P}$ in GS_{12} were specifically properties of the TSA conformation or a more general features of the domain closure. The model was built from the crystal structure of the βPGM_{D10N}−$\beta G16BP$ complex (PDB 5O6P), including the same atoms as those in the QM_{WT} PO_3 model (i.e., residue N10 was subsituted with protonated D10), and was optimized to establish the preferred atomic positions. The NAC III model established that when βPGM is in this conformation there is negligible transfer of HT1 to $O1_{G6P}$ (HT1−$O1_{G6P}$ = 1.93 Å and $OD2_{D10}$−HT1 = 0.98 Å) or dissociation of P1 from $O1_{G6P}$ ($O1_{G6P}$−$P1_{PO3}$ = 1.68 Å and $P1_{PO3}$−$OD1_{D8}$ = 3.22 Å). Hence, the transition of the enzyme between the NAC III and NAC II or TSA conformations, which delivers full domain closure, is required for the partial transfer of HT1 from $OD2_{D10}$ to $O1_{G6P}$ and the partial dissociation of P1 from $O1_{G6P}$.

D10N PGM QM model. To have a quantitative picture of the extent to which proton transfer interacts with phosphoryl transfer, a second QM model was made by substituting D10 for N10, which strongly resists proton transfer. Previous X-ray crystallographic investigations of a TSA complex containing this mutation (βPGM_{D10N}−AlF_4−G6P, PDB 5OK2, 1.1 Å)[18] suggest that the N10 carboxamide group is orientated so as to form a HT1−$O1_{G6P}$ hydrogen bond to a deprotonated $O1_{G6P}$ atom (Figure S13). This orientation (and protonation state) was therefore maintained in the QM_{D10N} PO_3 model. An exhaustive TS search was conducted to establish a new reaction path for this variant without success. During all attempts, preventing the substantial protonation of $O1_{G6P}$ caused a collapse back to a GS_{12}-like geometry. Instead, the wild-type reaction path was modified by the introduction of N10 at each step before the reoptimization and re-evaluation of single point energies (Figure 3). A near-linear increase in energy across the reaction coordinate was observed, and no stable TS_{23} or GS_{34} structures were found. In this QM_{D10N} PO_3 model, structures corresponding to the equivalent GS and TS points in the QM_{WT} PO_3 model (GS_{12}', TS_{23}', and GS_{34}') reveal a consistently large HT1−$O1_{G6P}$ distance (1.60 ± 0.1 Å), confirming that HT1 resists transfer to $O1_{G6P}$ throughout. Correspondingly, the energies of TS_{23}' and GS_{34}' relative to GS_{12}' (+102 and +118 kJ mol^{-1}, respectively) reveal that both structures were significantly destabilized compared with their wild-type equivalents.

IQA and REG Analysis. The single point energies of each geometry computed for both the QM_{WT} PO_3 and QM_{D10N} PO_3 models across the reaction coordinate are intrinsically a summation of all possible kinetic, electrostatic, exchange, and correlation intra- and interatomic energy terms. A number of popular schemes have been created with the goal of extracting chemical insights into these terms via energy decomposition.[30] In the present work, this chemical insight comes in the form of an understanding of which energy terms, and therefore

chemical groups, most strongly contribute to either the stabilization or destabilization of GS_{12}, TS_{23}, and GS_{34}, relative to one another. A full energy decomposition of each molecular wave function[31] in both the QM_{WT} PO_3 and QM_{D10N} PO_3 models was carried out using the interacting quantum atoms (IQA) methodology within the parameter-, orbital-, and reference-state-free quantum chemical topology (QCT) framework, which was implemented in AIMAll17.[32−35] IQA determines the electrostatic and exchange-correlation interactions between all possible atom pairs and also calculates the nonpairwise energies of each individual atom. As exchange-correlation energy terms correspond to covalent bond energies, the bond order is additionally determined (Equation S3.7).[36] Additionally, atomic net charges are clearly defined as the electron density within an atomic basin corrected for the nuclear charge. Overall, there are n^2 energy terms that sum to return the total energy of a system with n atoms, so our 163 atom QM_{WT} PO_3 model has 26 569 intra- and interatomic terms for each of the nine geometries across the reaction coordinate (26 896 for the 164 atom QM_{D10N} PO_3 model). The relative energy gradient (REG) method, which was implemented using the program ANANKE, was used to systematically rank these energy terms according to their individual contributions toward the behavior of an overall energy profile.[37−40] To do so, the gradient of a given energy term between any two chosen points was compared to the gradient of the total energy between those two points. Energy terms with the largest positive REG values behave most like the total system energy.

In the QM_{WT} PO_3 model, segments 2 and 3 of each reaction profile (corresponding to $GS_{12} \rightarrow TS_{23}$ and $TS_{23} \rightarrow GS_{34}$, respectively) are the main segments of interest as they directly relate to changes between stationary points. In Tables S5 and S6, the intra- and interatomic terms with the largest positive (reflecting the energy profile) and negative (opposing the energy profile) REG values for segments 2 and 3 of the QM_{WT} PO_3 and QM_{D10N} PO_3 models are reported, respectively, and the data are schematically represented in Figure 4. In segment 2 ($GS_{12} \rightarrow TS_{23}$) of the QM_{WT} PO_3 model, energy terms that raise the energy of the TS relative to the GS include electrostatic and covalent terms directly associated with $O1_{G6P}$−$P1_{PO3}$ bond lengthening (change in the bond order from 0.61 to 0.21, Figure 3). Further destabilization comes from $OD1_{D8}$−CD_{D8} bond lengthening, a reduction in the $P1_{PO3}$−CD_{D8} distance (increasing their electrostatic repulsion), and an increase in $OD2_{D10}$−$P1_{PO3}$ distance (reducing their electrostatic attraction). This destabilization is opposed not only by partial $P1_{PO3}$−$OD1_{D8}$ bond formation (change in the bond order from 0.06 to 0.36) but also by a reduction in the electrostatic repulsion between $P1_{PO3}$ and HT1 as the phosphoryl group leaves $O1_{G6P}$ and a reduction in the O−O electrostatic repulsion between all three PO_3^- oxygen atoms and $O1_{G6P}$. In segment 3 ($TS_{23} \rightarrow GS_{34}$), the destabilizing effects on GS_{34} relative to TS_{23} are similar to those in segment 2, with $O1_{G6P}$−$P1_{PO3}$ and $P1_{PO3}$−CD_{D8} electrostatic interactions dominating. PO_3^- oxygen atoms that significantly repel $OD1_{D8}$ provide additional destabilization. However, GS_{34} is more stable than TS_{23} largely due to formation of the $P1_{PO3}$−$OD1_{D8}$ bond (change in the bond order from 0.36 to 0.46) and a strong $P1_{PO3}$−$OD2_{D8}$ electrostatic attraction. The further reduction in the electrostatic repulsion between $P1_{PO3}$ and HT1 also remains a key element of GS_{34} stabilization in segment 3.
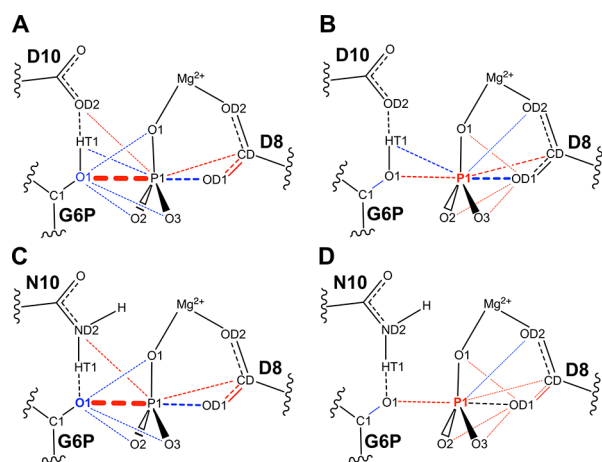
Figure 4. Schematic representation of the REG analysis. (A) QM_{WT} PO_3 model $GS_{12} \rightarrow TS_{23}$. (B) QM_{WT} PO_3 model $TS_{23} \rightarrow GS_{34}$. (C) QM_{D10N} PO_3 model $GS_{12}' \rightarrow TS_{23}'$. (D) QM_{D10N} PO_3 model $TS_{23}' \rightarrow GS_{34}'$. Red and blue colored dotted lines and atoms represent energy terms that contribute the most to the relative energies of ground and transition states. The width of the dashed line represents the size of the REG values (Tables S5 and S6). Red indicates that an energy term increases (becomes more positive or less negative) from $GS_{12} \rightarrow TS_{23}$ or $TS_{23} \rightarrow GS_{34}$. Blue indicates that the energy term decreases. The REG analysis identified two key differences between (A and B) the WT and (C and D) D10N. (i) In the WT, HT1 transfer to $O1_{G6P}$ results in electrostatic repulsion between HT1 and $P1_{PO3}$. As $P1_{PO3}$ is transferred to D8, this repulsion is alleviated. (ii) Greater negative charge density on ND2 relative to OD2 results in a greater electrostatic attraction with $P1_{PO3}$. As $P1_{PO3}$ is transferred to D8, this attractive stabilizing interaction is therefore reduced more in D10N than in the WT.

In the QM_{D10N} PO_3 model reaction path, disfavoring the transfer of HT1 to $O1_{G6P}$ is classically expected to cause a significant buildup of electron density on $O1_{G6P}$ as the phosphoryl group departs, changing from an initial partial negative charge to a formal negative charge upon complete breakage of the $O1_{G6P}-P1_{PO3}$ bond. A greater $O1_{G6P}$ negative charge would substantially increase all of its electrostatic interactions and consequently play a large role in the observed overall destabilization in its reaction path. In GS_{12}', $O1_{G6P}$ has a -1.20 e charge density and a $HT1-O1_{G6P}$ bond order of 0.22 (Figure 3); however, in GS_{12}, $O1_{G6P}$ has a -1.23 e charge density, despite a closer HT1 atom (1.12 versus 1.50 Å), and a $HT1-O1_{G6P}$ bond order of 0.41 (Tables S2 and S3). Hence, the charge of $O1_{G6P}$ is not significantly impacted by the position of the GAB proton. An inspection of the energy terms related to $O1_{G6P}$ in segment 2 of the QM_{D10N} PO_3 model $(GS_{12}' \rightarrow TS_{23}')$ reveals only minor differences ($<3\%$) between both stabilizing and destabilizing $O1_{G6P}$ interactions compared to those in the $QM_{WT}PO_3$ model. All other major interactions are also similar to those in the $QM_{WT}PO_3$ model. The key differences between models arise from $D10-P1_{PO3}$ or $N10-P1_{PO3}$ electrostatic interactions. First, $ND2_{N10}$ has a greater negative charge density (-1.29 e) in GS_{12}' than $OD2_{D10}$ in GS_{12} (-1.22 e) (Tables S2 and S3). As a result, the $ND2_{D10}-P1_{PO3}$ electrostatic attraction is relatively higher so that the increase in the $ND2_{D10}-P1_{PO3}$ separation during progress towards TS_{23}' results in additional destabilization relative to the wild-type. Second, the $HT1-P1_{PO3}$ electrostatic repulsion is less affected during progress towards TS_{23}' in the $QM_{D10N}PO_3$ model (from 2.87 to 3.47 Å) than during progress

toward TS_{23} in the $QM_{WT}PO_3$ model (from 2.50 to 2.98 Å). The alleviation of this repulsion is a primary contributor to the relatively small energy difference between TS_{23} and GS_{12}. Therefore, TS stabilization by the GAB residue involves the balance of the attractive and repulsive interactions of the transferring phosphorus atom with the GAB donor atom and the donated proton, respectively, rather than the protonation state of $O1_{G6P}$.

Calculation of Experimental Parameters. The QM PO_3 models allow us to conclude that proton transfer is a fundamental early step in the cleavage of the $O1_{G6P}-P1_{PO3}$ bond, which is stimulated to a large extent by the change in the enzyme conformation from NAC III to NAC II or TSA. Such a conclusion, however, is reliant on the QM models being appropriate descriptions of enzyme behavior; thus, further experimental validation was sought. This cannot be readily obtained using ground-state and ground-state analogue measurements since previous studies of the pre- and postphosphoryl transfer ground state species (the $\beta PGM_{WT}-$BeF$_3-$G6P complex[5] and the $\beta PGM_{D10N}-\beta G16BP$ complex,[18] respectively) have indicated that there is a significant relaxation of the enzyme away from its TSA conformation. Hence, a direct comparison with the higher energy states GS_{12} and GS_{34} is not appropriate. However, experimental validation can be achieved against measurements of TSA complexes with and without mutations (using the $\beta PGM_{WT}-AlF_4-G6P$[17] and $\beta PGM_{D10N}-AlF_4-G6P$ complexes[18]), where the enzyme conformation closely matches that in the QM models. Correspondingly, QM models of these TSA complexes were made to determine any variations in the local structure that might be diagnostic of a particular complex and to compute ^{19}F chemical shifts, which are readily accessible experimentally.[6,9]

In the QM_{WT} PO_3 model, PO_3^- was resubstituted for AlF_4^- to generate the QM_{WT} AlF_4 model. As the model was reoptimized to a ground state rather than a transition state, the computational demand decreased, allowing for 10 additional distal amino acid residues (G11, V12, T16, A17, H20, K45, S48, A113, S116, and S171) to be included so that the final model contained 386 atoms (Figure S4). NMR-derived order parameters (S^2 values) for the $\beta PGM_{WT}-AlF_4-G6P$ complex were again used to guide boundary positions; fixed backbone atoms were always ≤ 2 atoms from a well ordered ($S^2 \geq 0.8$) amide (Table S7). The same procedure was carried out to convert the QM_{D10N} PO_3 model to a QM_{D10N} AlF_4 model. An additional QM_{D10N} AlF_4 model was created in which $O1_{G6P}$ was protonated, since previous experimental approaches[18] did not explicitly determine the protonation state of $O1_{G6P}$ in the $\beta PGM_{D10N}-AlF_4-G6P$ complex. Upon the optimization of the protonated QM_{D10N} AlF_4 model, the $HT1-O1_{G6P}$ hydrogen bond was maintained but lengthened (from 1.79 to 2.09 Å) compared with that in the deprotonated model, and the additional hydrogen was oriented toward the hydroxyl group of residue S114. In all cases, the agreement between computed TSA model architectures and the enzyme conformation in crystallographic TSA complexes was excellent (Figures S4–S6). In the deprotonated QM_{D10N} AlF_4 model, a distortion of the average $O1_{G6P}-Al-F_x$ angle by $+4.6°$ was observed relative to that in the QM_{WT} AlF_4 model (94.3° vs 89.8°, respectively), with the $O1_{G6P}-Al$ distance decreased (from 2.00 to 1.85 Å, Figure S7). In the protonated QM_{D10N} AlF_4 model, an opposite distortion of the average $O1_{G6P}-Al-F_x$ angle by $-3.3°$ was observed relative to that in the QM_{WT} AlF_4 model
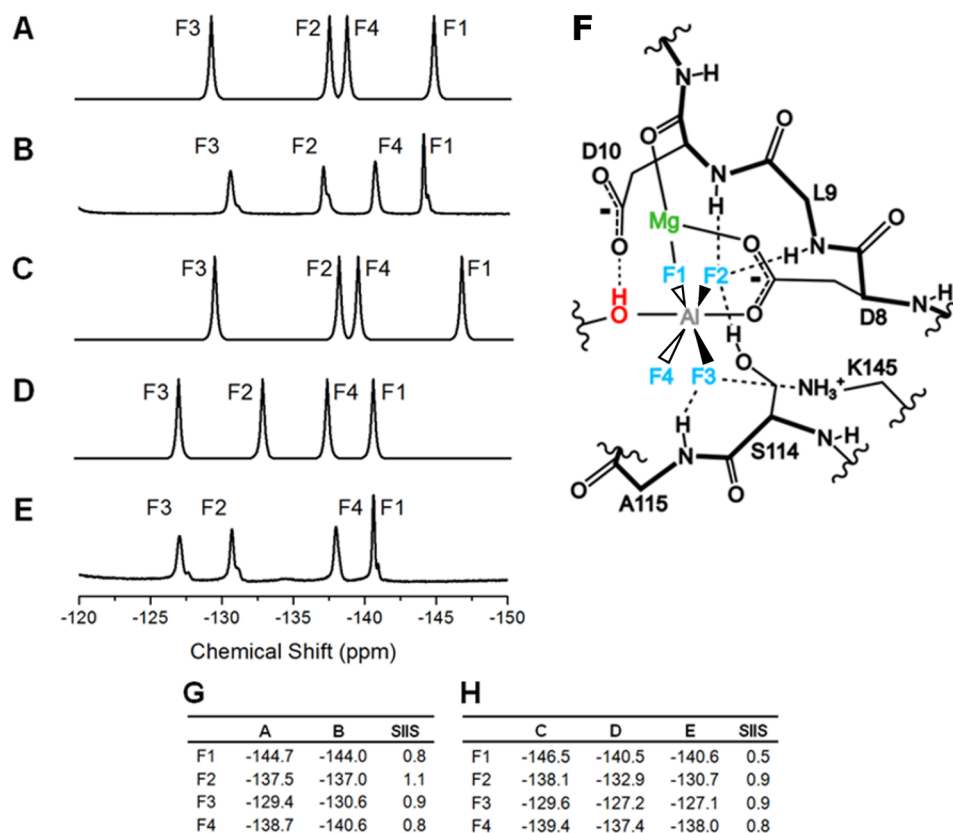
Figure 5. Comparison of experimental and calculated fluorine shifts for βPGM_{WT} and βPGM_{D10N}–AlF$_4$–G6P complexes. (A) Calculated ^{19}F 1D NMR spectrum of the QM$_{WT}$ AlF$_4$ model, (B) experimental ^{19}F 1D NMR spectrum of the βPGM_{WT}–AlF$_4$–G6P complex in 90% H$_2$O and 10% D$_2$O, (C) calculated ^{19}F 1D NMR spectrum of QM$_{D10N}$ AlF$_4$ model with O1$_{G6P}$ protonated, (D) calculated ^{19}F 1D NMR spectrum of QM$_{D10N}$ AlF$_4$ model with O1$_{G6P}$ deprotonated, (E) experimental ^{19}F 1D NMR spectrum of βPGM_{D10N}–AlF$_4$–G6P complex in 90% H$_2$O and 10% D$_2$O, and (F) an active-site schematic to correlate fluorine label and geometric position. (G) Calculated and experimental chemical shifts for the βPGM_{WT}–AlF$_4$–G6P complex (spectra A and B), and (H) calculated and experimental chemical shifts for the βPGM_{D10N}–AlF$_4$–G6P complex (spectra C, D and E) are presented alongside solvent induced isotope shift (SIIS) values for each of the resonances.

(86.5° vs 89.8°, respectively), with the O1$_{G6P}$-Al distance increased (from 2.00 to 2.15 Å, Figure S7). Computed ^{19}F NMR chemical shift changes between the two complexes reveal an average downfield chemical shift change, relative to the wild-type, of 3.1 ppm in the deprotonated QM$_{D10N}$ AlF$_4$ model and an average upfield chemical shift change of 0.8 ppm in the protonated QM$_{D10N}$ AlF$_4$ model (Figure 5). It was also apparent that in the QM$_{WT}$ AlF$_4$ model the GAB proton, HT1, was not solely associated with O1$_{G6P}$ (1.03 Å, bond order of 0.56) and had a partial association with OD2$_{D10}$ (1.56 Å, bond order of 0.23).

Structure of the βPGM_{D10N}–AlF$_4$–G6P Complex. Experimental validation of the βPGM_{D10N}–AlF$_4$–G6P complex models relies on the assumption that the N10 carboxamide is oriented so as to form a HT1–O1$_{G6P}$ hydrogen bond rather than the opposite rotamer, where O1$_{G6P}$ is protonated and forms a OD1$_{N10}$–HT1 hydrogen bond. This assumption was not previously explicitly tested in the structure of the βPGM_{D10N}–AlF$_4$–G6P complex (PDB 5OK2[18]). Rerefinement of the N10 carboxamide in the opposite orientation yielded a difference map peak of >3σ for the alternately modeled atoms (Figure S13), indicating that the carboxamide indeed adopts the previously assumed orientation. A crystal of the βPGM_{D10N}–AlF$_4$–G6P complex at a higher resolution (1.02 Å) corroborates this interpretation and further supports a model where the O1$_{G6P}$ atom is

deprotonated (PDB 6L03; Figure S14). The higher-resolution structure revealed an out-of-plane distortion of the Al^{3+} atom of the AlF$_4^-$ group of +3° toward the O1$_{G6P}$ atom. A re-examination of 5OK2 indicates that this distortion is also present in the lower-resolution structure, but the angle of distortion cannot be defined as accurately. In both cases, the O1$_{G6P}$–Al distance is shorter than that of Al–OD1$_{D8}$ by ca. 0.15 Å (Figure S7). In the WT complex crystal, no distortion from the planarity of the AlF$_4^-$ was observed within error. These experimental observations are in excellent agreement with the computed distortion of +4.6° in the deprotonated QM$_{D10N}$ AlF$_4$ model and the computed absence of distortion in the QM$_{WT}$ AlF$_4$ model and therefore provide validation of the QM models used throughout.

NMR Spectroscopy of the βPGM_{D10N}–AlF$_4$–G6P Complex. The βPGM_{D10N}–AlF$_4$–G6P complex has not been studied extensively using solution NMR methods compared with the βPGM_{WT}–AlF$_4$–G6P complex.[10,17] Therefore, the βPGM_{D10N}–AlF$_4$–G6P complex was prepared as described previously,[17,18] and a 97% backbone assignment of non-proline residues was determined (BMRB 27697). The chemical shifts were compared to those of the previously assigned βPGM_{WT}–AlF$_4$–G6P complex (BMRB 15467),[10] and only subtle chemical shift perturbations (CSPs) were observed. These CSPs occurred in four distinct regions, each of which was in direct contact with the substrate (Figure S8).

This indicates that the enzyme conformation and the accommodation of substrate in the active site are very similar in the two complexes. NMR relaxation measurements of fast (picosecond to nanosecond) dynamics corroborate this interpretation, with few significant differences in the observed order parameters (Figure S9). Almost all of the discernible changes are distant from the active site and are juxtaposed to changes of the opposite sign, which is indicative of local compensatory mechanisms (Figures S9–S11).

An average downfield chemical shift change of 4.0 ppm was observed in the 1D ^{19}F NMR spectra for AlF$_4^-$ peaks in the βPGM$_{D10N}$–AlF$_4$–G6P complex as compared with the βPGM$_{WT}$–AlF$_4$–G6P complex (Figure 5). This is in excellent agreement with the predicted average downfield shift (3.1 ppm) in the deprotonated QM$_{D10N}$ AlF$_4$ model, providing further strong support for a deprotonated O1$_{G6P}$ atom in this complex and validating the deprotonation in the QM$_{D10N}$ PO$_3$ model. The hydrogen bonding to the fluorides in the two complexes was assessed using ^{19}F solvent-induced isotope shifts (SIIS), which are highly sensitive to the distance between hydrogen bonding partners and the fluoride ions.[17] The SIIS values for the βPGM$_{D10N}$–AlF$_4$–G6P complex mirror those of the βPGM$_{WT}$–AlF$_4$–G6P complex and, while there is a small overall reduction in SIIS values (ca. 0.1 ppm), are consistent with only minor changes in hydrogen bonding between the enzyme and the AlF$_4^-$ group following mutation (Figure S12, Tables S9–S11). Hence, such changes can be eliminated as the primary source of the average downfield chemical shift change between the two complexes.

In the βPGM$_{WT}$–AlF$_4$–G6P complex, ^{13}C chemical shift measurements indicate that the GAB proton, HT1, is not solely associated with O1$_{G6P}$ (Table S12). For example, the Cβ ^{13}C chemical shift of D10 is the most upfield of all Asp residues in this complex, implying some degree of protonation (Table S8). It is ca. 2 ppm upfield compared to that in the βPGM$_{WT}$–BeF$_3^-$ complex, which is more open and has the D10 residue rotated out of the active site (Table S8).[5] However, it is only 0.44 ppm upfield of the equivalent resonance of D180 in the βPGM$_{WT}$–AlF$_4$–G6P complex, which is surface-exposed and likely to be deprotonated at the experimental pH. Together, this indicates that some sharing of the GAB proton between atoms O1$_{G6P}$ and OD2$_{D10}$ in the βPGM$_{WT}$–AlF$_4$–G6P complex occurs, which is again in excellent agreement with the QM$_{WT}$ AlF$_4$ model.

Charge Densities during Phosphoryl Transfer. The close agreement between the experiments and QM models allows further inferences to be made by comparing the two PO$_3$ and three AlF$_4$ models. First, the extent of proton transfer from the GAB to the sugar in the QM$_{WT}$ AlF$_4$ model and for TS$_{23}$ in the QM$_{WT}$ PO$_3$ model is very similar (HT1–O1$_{G6P}$ = 1.03 or 1.04 Å and OD2$_{D10}$–HT1 = 1.56 or 1.51 Å, respectively), further extending the value of AlF$_4$ complexes as TSAs (Table S4). There is also a strong similarity in the charge density associated with O1$_{G6P}$ in the two models (QM$_{WT}$ AlF$_4$ model = −1.14 e and TS$_{23}$ = −1.16 e). However, these parameters do not have a simple relationship; for example, O1$_{G6P}$ is more negative in GS$_{12}$ (−1.23 e), whereas the extent of proton transfer from the GAB to the sugar is lower (HT1–O1$_{G6P}$ = 1.12 Å and OD2$_{D10}$–HT1 = 1.33 Å). Second, the primary influence on the O1$_{G6P}$ charge density in the AlF$_4$ models is the O1$_{G6P}$–Al distance. O1$_{G6P}$ becomes more negative (from −1.14 to −1.24 e) as the O1$_{G6P}$–Al distance shortens (from 2.00 to 1.85 Å). The Al charge density

remains constant (2.65 ± 0.01 e), and the change in O1$_{G6P}$ occurs primarily at the expense of C1$_{G6P}$ (from 0.82 to 0.88 e). Also including the data from the protonated QM$_{D10N}$ AlF$_4$ model, the effect on the O1$_{G6P}$ charge density is modeled well by simple Coulombic competition, where the Al atom augments the electronegativity of O1$_{G6P}$. The same effect was found between the O1$_{G6P}$ charge density (from −1.16 to −1.23 e) and the O1$_{G6P}$–P1$_{PO_3}$ distance (2.43 → 1.85 Å) when comparing TS$_{23}$ and GS$_{12}$ in the PO$_3$ models. Indeed, these parameters become matched in the QM$_{D10N}$ AlF$_4$ model and for GS$_{12}$ in the QM$_{WT}$ PO$_3$ model (−1.24 or −1.23 e and 1.85 or 1.85 Å, respectively). In essence, the nucleophilicity of an axial oxygen atom becomes stronger the closer it is to the transferring phosphorus atom. The competition for electron density between the phosphorus atom and the approaching nucleophilic oxygen has the potential to lower the barrier for phosphoryl transfer. An increase in the positive charge on the phosphorus atom will partially compensate for the energy increase associated with its movement away from the leaving group oxygen. This points to a scenario whereby it is valuable that an enzyme closely complements the balance between the gains associated with a nucleophile closer to the leaving group oxygen distance and the costs associated with increased oxygen–oxygen repulsion.

■ DISCUSSION

Proton and Phosphoryl Transfer Triggered by the Adoption of a TSA Architecture. The combination of QM models, X-ray structures, and NMR measurements points toward a balance between proton transfer from the GAB residue and the promotion of phosphoryl transfer. Both these processes are assisted by the transition of the enzyme from the NAC III conformation to the NAC II or TSA conformation via a 13° relative rotation of the cap and core domains, which is in line with the βPGM–βG16BP complex (PDB 5OK1) preferring to adopt the NAC III conformation.[18] This final closure of the two domains is associated with the substantial transfer of the GAB proton from the GAB residue (residual bond order of 0.34) to the leaving group oxygen atom of the sugar (bond order of 0.41), which is combined with the partial dissociation of the P–O bond with the sugar (residual bond order 0.61). The corollary to this is that phosphoryl and proton transfer therefore benefit from a change in the enzyme conformation, strongly implicating the enzyme conformational change between alternatively closed structures to be instrumental in the catalysis of phosphoryl transfer in βPGM. Given the time scale differences between enzyme conformational fluctuations and bond vibrations, this conformational fluctuation is likely to be the instigating event in phosphoryl transfer.

Phosphoryl Transfer Driven by H–P Repulsion. While the QM models indicate that proton transfer is an important step to initiate phosphoryl transfer, this is not via stabilization of the developing negative charge on the leaving group oxygen. The charge density on O1$_{G6P}$ is in fact similar in the QM$_{WT}$ PO$_3$ and QM$_{D10N}$ PO$_3$ models despite the significant differences in the positioning of the GAB proton. Instead, electrostatic repulsion between the GAB proton and the transferring phosphorus atom provides a substantial stimulus for P–O bond dissociation. The reduction of this repulsive interaction when going from GS$_{12}$ to TS$_{23}$ helps to stabilize the transition state relative to the ground state. Correspondingly, the GS$_{12}'$ → TS$_{23}'$ transition in the QM$_{D10N}$ PO$_3$ model does

not benefit from a reduction of this repulsion to the same extent when proton transfer to $O1_{G6P}$ is resisted by N10.

AlF_4 Distortion Is a Reporter of Charge Distribution in the Active Site. Since the AlF_4^- moieties in TSA complexes are predominantly ionic species, they are less predisposed by covalency to particular geometries in the active site of phosphoryl transfer enzymes. Hence, they have the potential to report, through their distortion, which axial interactions have the stronger overall effect. The AlF_4^- moiety in the βPGM_{WT}–AlF_4–G6P complex shows no distortion from planarity in either the QM_{WT} AlF_4 model or the crystal structure, implying that the attraction and repulsion of the Al atom provided by the two axial groups is balanced by the extent of the proton transfer between the sugar and the GAB residue. The corollary of these observations is that significant proton transfer from the GAB residue to the leaving group oxygen atom is required for the AlF_4^- mimic of the transferring phosphoryl group to be the most stable in a planar form. This is consistent with an early proton transfer event stabilizing a planar phosphoryl group during phosphoryl transfer from βG16BP to D8 in the native reaction. In the βPGM_{D10N}–AlF_4–G6P complex, the GAB proton does not transfer significantly to the sugar and thus does not electrostatically repel the Al atom (and by extension the P atom in the native reaction) to the same extent. Hence, the AlF_4^- moiety is not planar in this complex.

The original QM study of phosphoryl transfer in βPGM,[21] which used 103 B3LYP atoms (390 total atoms) and a DFT/PM3MM approach to calculate energy terms, predicted an early proton transfer step as part of a concerted transition state for the reaction with an energy barrier of 40.6 kJ mol^{-1} for phosphoryl transfer from βG16BP to D8. Such behavior was supported by a subsequent QM/MM study,[22] though a higher energy was calculated (55.2 to 59.9 kJ mol^{-1}). However, a different QM/MM study[24] asserted that βPGM had a dissociated pentacoordinate phosphorane transition state with a late proton transfer event corresponding to an energy barrier of 46.4 kJ mol^{-1}. Most recently, phosphoryl transfer within βPGM was examined using an EVB approach based on a 43 atom core,[23] which predicted both a concerted transition state and a concerted proton transfer event in addition to an energy barrier of 60.3 kJ mol^{-1}. The present study provides further support that βPGM proton transfer and phosphoryl transfer are concerted events and indeed are strongly favored by the NAC III or NAC I to NAC II or TSA conformational transitions.

In conclusion, the excellent agreement between NMR- and X-ray-determined parameters and their predicted values in the corresponding QM models provides substantial confidence in the quantitation of the calculated phosphoryl transfer reaction paths. The competition between the GAB proton and the P atom for the leaving group oxygen strongly manifests through their mutual repulsion. The transformation of the enzyme into its fully closed conformation and the corresponding positioning of the GAB functionality adjacent to the leaving group oxygen stimulate partial proton transfer, intensify this mutual repulsion, and promote phosphoryl transfer. In the reverse direction, the formation of the P–O bond with the sugar stimulates the repulsion of the GAB proton and hence an enzyme conformational change away from the fully closed conformation. The reduced atomic charges and low covalency in metal fluoride mimics of phosphoryl groups make them highly sensitive experimental reporters of these antagonisms within the active-site charge distribution beyond just reporting on the electrostatic interactions of the axial oxygen atoms. Together, the synergy between experimental and computational approaches thus reveals the exquisite balance between GAB atoms and phosphoryl transfer and the associated modulation of the charge distribution.

■ ASSOCIATED CONTENT

⊕ Supporting Information

The Supporting Information is available free of charge at https://pubs.acs.org/doi/10.1021/acscatal.1c01389.

Animation of the reaction path (GIF)

Materials and methods, Figures S1–S14, Tables S1–S13, and supporting references (PDF)

Constrained optimized geometry for AlF_4 model (XYZ)

Constrained optimized geometry for AlF_4 model (XYZ)

Constrained optimized geometry from the reaction path (PDB)

Constrained optimized geometry from the reaction path (PDB)

Constrained optimized geometry from the reaction path (PDB)

Constrained optimized geometry from the reaction path (PDB)

Constrained optimized geometry from the reaction path (PDB)

Constrained optimized geometry from the reaction path (PDB)

Constrained optimized geometry from the reaction path (PDB)

Constrained optimized geometry from the reaction path (PDB)

Constrained optimized geometry from the reaction path (PDB)

Accession Codes

The atomic coordinates and structure factors have been deposited in the Protein Data Bank (www.rcsb.org) with the following PDB codes: βPGM_{D10N}–AlF4–G6P complex (1.10 Å), 5OK2; βPGM_{D10N}–AlF4–G6P complex (1.02 Å), 6L03. The NMR chemical shifts have been deposited in the BioMagResBank (www.bmrb.wisc.edu) with the accession number 27697

■ AUTHOR INFORMATION

Corresponding Author

Jonathan P. Waltho − *Department of Molecular Biology and Biotechnology, Krebs Institute for Biomolecular Research, The University of Sheffield, Sheffield S10 2TN, United Kingdom; Department of Chemistry, Manchester Institute of Biotechnology, The University of Manchester, Manchester M1 7DN, United Kingdom;* ⊙ orcid.org/0000-0002-7402-5492; Email: j.waltho@sheffield.ac.uk

Authors

Angus J. Robertson − *Department of Molecular Biology and Biotechnology, Krebs Institute for Biomolecular Research, The University of Sheffield, Sheffield S10 2TN, United Kingdom; Present Address: Laboratory of Chemical Physics, National Institute of Diabetes and Digestive and Kidney Diseases, National Institutes of Health, Bethesda, MD 20892, USA*

Alex L. Wilson − *Department of Chemistry, Manchester Institute of Biotechnology, The University of Manchester, Manchester M1 7DN, United Kingdom*

Matthew J. Burn − *Department of Chemistry, Manchester Institute of Biotechnology, The University of Manchester, Manchester M1 7DN, United Kingdom*

Matthew J. Cliff − *Department of Chemistry, Manchester Institute of Biotechnology, The University of Manchester, Manchester M1 7DN, United Kingdom*

Paul L. A. Popelier − *Department of Chemistry, Manchester Institute of Biotechnology, The University of Manchester, Manchester M1 7DN, United Kingdom*

Complete contact information is available at:
https://pubs.acs.org/10.1021/acscatal.1c01389

Author Contributions

[⊥]These authors contributed equally. The manuscript was written through contributions of all authors. All authors have given approval to the final version of the manuscript.

Notes

The authors declare no competing financial interest.

■ REFERENCES

(1) Knowles, J. R. Enzyme-Catalyzed Phosphoryl Transfer Reactions. *Annu. Rev. Biochem.* **1980**, *49*, 877.

(2) Lad, C.; Williams, N. H.; Wolfenden, R. The rate of hydrolysis of phosphomonoester dianions and the exceptional catalytic proficiencies of protein and inositol phosphatases. *Proc. Natl. Acad. Sci. U. S. A.* **2003**, *100*, 5607.

(3) Cleland, W. W.; Hengge, A. C. Enzymatic Mechanisms of Phosphate and Sulfate Transfer. *Chem. Rev.* **2006**, *106*, 3252.

(4) Lassila, J. K.; Zalatan, J. G.; Herschlag, D. Biological Phosphoryl-Transfer Reactions: Understanding Mechanism and Catalysis. *Annu. Rev. Biochem.* **2011**, *80*, 669.

(5) Griffin, J. L.; Bowler, M. W.; Baxter, N. J.; Leigh, K. N.; Dannatt, H. R. W.; Hounslow, A. M.; Blackburn, G. M.; Webster, C. E.; Cliff, M. J.; Waltho, J. P. Near attack conformers dominate β-phosphoglucomutase complexes where geometry and charge distribution reflect those of substrate. *Proc. Natl. Acad. Sci. U. S. A.* **2012**, *109*, 6910.

(6) Jin, Y.; Richards, N. G.; Waltho, J. P.; Blackburn, G. M. Metal Fluorides as Analogues for Studies on Phosphoryl Transfer Enzymes. *Angew. Chem., Int. Ed.* **2017**, *56*, 4110.

(7) Westheimer, F. H. Why nature chose phosphates. *Science* **1987**, *235*, 1173.

(8) Kamerlin, S. C. L.; Sharma, P. K.; Prasad, R. B.; Warshel, A. Why nature really chose phosphate. *Q. Rev. Biophys.* **2013**, *46*, 1.

(9) Jin, Y.; Molt Jr, R. W.; Pellegrini, E.; Cliff, M. J.; Bowler, M. W.; Richards, N. G. J.; Blackburn, G. M.; Waltho, J. P. Assessing the Influence of Mutation on GTPase Transition States by Using X-ray Crystallography, 19F NMR, and DFT Approaches. *Angew. Chem., Int. Ed.* **2017**, *56*, 9732.

(10) Baxter, N. J.; Blackburn, G. M.; Marston, J. P.; Hounslow, A. M.; Cliff, M. J.; Bermel, W.; Williams, N. H.; Hollfelder, F.; Wemmer, D. E.; Waltho, J. P. Anionic Charge Is Prioritized over Geometry in Aluminum and Magnesium Fluoride Transition State Analogs of Phosphoryl Transfer Enzymes. *J. Am. Chem. Soc.* **2008**, *130*, 3952.

(11) Cliff, M. J.; Bowler, M. W.; Varga, A.; Marston, J. P.; Szabó, J.; Hounslow, A. M.; Baxter, N. J.; Blackburn, G. M.; Vas, M.; Waltho, J. P. Transition State Analogue Structures of Human Phosphoglycerate Kinase Establish the Importance of Charge Balance in Catalysis. *J. Am. Chem. Soc.* **2010**, *132*, 6507.

(12) Lahiri, S. D.; Zhang, G.; Dai, J.; Dunaway-Mariano, D.; Allen, K. N. Analysis of the Substrate Specificity Loop of the HAD Superfamily Cap Domain. *Biochemistry* **2004**, *43*, 2812.

(13) Zhang, G.; Dai, J.; Wang, L.; Dunaway-Mariano, D.; Tremblay, L. W.; Allen, K. N. Catalytic Cycling in β-Phosphoglucomutase: A Kinetic and Structural Analysis. *Biochemistry* **2005**, *44*, 9404.

(14) Dai, J.; Finci, L.; Zhang, C.; Lahiri, S.; Zhang, G.; Peisach, E.; Allen, K. N.; Dunaway-Mariano, D. Analysis of the Structural Determinants Underlying Discrimination between Substrate and Solvent in β-Phosphoglucomutase Catalysis. *Biochemistry* **2009**, *48*, 1984.

(15) Dai, J.; Wang, L.; Allen, K. N.; Radstrom, P.; Dunaway-Mariano, D. Conformational Cycling in β-Phosphoglucomutase Catalysis: Reorientation of the β-d-Glucose 1,6-(Bis)phosphate Intermediate. *Biochemistry* **2006**, *45*, 7818.

(16) Baxter, N. J.; Olguin, L. F.; Goličnik, M.; Feng, G.; Hounslow, A. M.; Bermel, W.; Blackburn, G. M.; Hollfelder, F.; Waltho, J. P.; Williams, N. H. A Trojan horse transition state analogue generated by MgF$_3^-$ formation in an enzyme active site. *Proc. Natl. Acad. Sci. U. S. A.* **2006**, *103*, 14732.

(17) Baxter, N. J.; Bowler, M. W.; Alizadeh, T.; Cliff, M. J.; Hounslow, A. M.; Wu, B.; Berkowitz, D. B.; Williams, N. H.; Blackburn, G. M.; Waltho, J. P. Atomic details of near-transition state conformers for enzyme phosphoryl transfer revealed by MgF$_3^-$ rather than by phosphoranes. *Proc. Natl. Acad. Sci. U. S. A.* **2010**, *107*, 4555.

(18) Johnson, L. A.; Robertson, A. J.; Baxter, N. J.; Trevitt, C. R.; Bisson, C.; Jin, Y.; Wood, H. P.; Hounslow, A. M.; Cliff, M. J.; Blackburn, G. M.; Bowler, M. W.; Waltho, J. P. van der Waals Contact between Nucleophile and Transferring Phosphorus Is Insufficient To Achieve Enzyme Transition-State Architecture. *ACS Catal.* **2018**, *8*, 8140.

(19) Goličnik, M.; Olguin, L. F.; Feng, G.; Baxter, N. J.; Waltho, J. P.; Williams, N. H.; Hollfelder, F. Kinetic Analysis of β-Phosphoglucomutase and Its Inhibition by Magnesium Fluoride. *J. Am. Chem. Soc.* **2009**, *131*, 1575.

(20) Jin, Y.; Bhattasali, D.; Pellegrini, E.; Forget, S. M.; Baxter, N. J.; Cliff, M. J.; Bowler, M. W.; Jakeman, D. L.; Blackburn, G. M.; Waltho, J. P. α-Fluorophosphonates reveal how a phosphomutase conserves transition state conformation over hexose recognition in its two-step reaction. *Proc. Natl. Acad. Sci. U. S. A.* **2014**, *111*, 12384.

(21) Webster, C. E. High-Energy Intermediate or Stable Transition State Analogue: Theoretical Perspective of the Active Site and Mechanism of β-Phosphoglucomutase. *J. Am. Chem. Soc.* **2004**, *126*, 6840.

(22) Marcos, E.; Field, M. J.; Crehuet, R. Pentacoordinated phosphorus revisited by high-level QM/MM calculations. *Proteins: Struct., Funct., Genet.* **2010**, *78*, 2405−2411.

(23) Barrozo, A.; Liao, Q.; Esguerra, M.; Marloie, G.; Florián, J.; Williams, N. H.; Kamerlin, S. C. L. Computer simulations of the catalytic mechanism of wild-type and mutant β-phosphoglucomutase. *Org. Biomol. Chem.* **2018**, *16*, 2060.

(24) Elsässer, B.; Dohmeier-Fischer, S.; Fels, G. Theoretical investigation of the enzymatic phosphoryl transfer of β-phosphoglucomutase: revisiting both steps of the catalytic cycle. *J. Mol. Model.* **2012**, *18*, 3169.

(25) Becke, A. D. Density-functional thermochemistry. III. The role of exact exchange. *J. Chem. Phys.* **1993**, *98*, 5648−5652.

(26) Lee, C.; Yang, W.; Parr, R. G. Development of the Colle-Salvetti correlation-energy formula into a functional of the electron density. *Phys. Rev. B: Condens. Matter Mater. Phys.* **1988**, *37*, 785.

(27) Vosko, S. H.; Wilk, L.; Nusair, M. Accurate spin-dependent electron liquid correlation energies for local spin density calculations: a critical analysis. *Can. J. Phys.* **1980**, *58*, 1200.

(28) Stephens, P. J.; Devlin, F. J.; Chabalowski, C. F.; Frisch, M. J. Ab initio calculation of vibrational absorption and circular dichroism spectra using density functional force fields. *J. Phys. Chem.* **1994**, *98*, 11623.

(29) Frisch, M. J.; Trucks, G. W.; Schlegel, H. B.; Scuseria, G. E.; Robb, M. A.; Cheeseman, J. R.; Scalmani, G.; Barone, V.; Mennucci, B.; Petersson, G. A.; Nakatsuji, H.; Caricato, M.; Li, X.; Hratchian, H. P.; Izmaylov, A. F.; Bloino, J.; Zheng, G.; Sonnenberg, J. L.; Hada, M.; Ehara, M.; Toyota, K.; Fukuda, R.; Hasegawa, J.; Ishida, M.; Nakajima, T.; Honda, Y.; Kitao, O.; Nakai, H.; Vreven, T.; Montgomery, J. A.; Peralta, J. E.; Ogliaro, F.; Bearpark, M.; Heyd, J. J.; Brothers, E.; Kudin, K. N.; Staroverov, V. N.; Kobayashi, R.; Normand, J.; Raghavachari, K.; Rendell, A.; Burant, J. C.; Iyengar, S. S.; Tomasi, J.; Cossi, M.; Rega, N.; Millam, J. M.; Klene, M.; Knox, J. E.; Cross, J. B.; Bakken, V.; Adamo, C.; Jaramillo, J.; Gomperts, R.; Stratmann, R. E.; Yazyev, O.; Austin, A. J.; Cammi, R.; Pomelli, C.; Ochterski, J. W.; Martin, R. L.; Morokuma, K.; Zakrzewski, V. G.; Voth, G. A.; Salvador, P.; Dannenberg, J. J.; Dapprich, S.; Daniels, A. D.; Farkas Foresman, J. B.; Ortiz, J. V.; Cioslowski, J.; Fox, D. J. *Gaussian 09*; Gaussian Inc: Wallingford, CT, 2009.

(30) Phipps, M. J. S.; Fox, T.; Tautermann, C. S.; Skylaris, C.-K. Energy decomposition analysis approaches and their evaluation on prototypical protein-drug interaction patterns. *Chem. Soc. Rev.* **2015**, *44*, 3177.

(31) Maxwell, P.; Pendás, A. M.; Popelier, P. L. A. Extension of the interacting quantum atoms (IQA) approach to B3LYP level density functional theory (DFT). *Phys. Chem. Chem. Phys.* **2016**, *18*, 20986−21000.

(32) Bader, R. *Atoms in molecules: A quantum theory.*; Oxford University Press: Oxford, U.K., 1994.

(33) Bader, R. F. W.; Anderson, S. G.; Duke, A. J. Quantum topology of molecular charge distributions. 1. *J. Am. Chem. Soc.* **1979**, *101*, 1389.

(34) Blanco, M. A.; Martín Pendás, A.; Francisco, E. Interacting quantum atoms: A correlated energy decomposition scheme based on the quantum theory of atoms in molecules. *J. Chem. Theory Comput.* **2005**, *1*, 1096.

(35) Keith, T. *AIMAll*; TK Gristmill Software: Overland Park, KS, 2017.

(36) Outeiral, C.; Vincent, M. A.; Martín Pendás, Á.; Popelier, P. L. A. Revitalizing the concept of bond order through delocalization measures in real space. *Chem. Sci.* **2018**, *9*, 5517.

(37) Thacker, J. C. R.; Popelier, P. L. A. Fluorine Gauche Effect Explained by Electrostatic Polarization Instead of Hyperconjugation: An Interacting Quantum Atoms (IQA) and Relative Energy Gradient (REG) Study. *J. Phys. Chem. A* **2018**, *122*, 1439.

(38) Thacker, J. C. R.; Vincent, M. A.; Popelier, P. L. A. Using the relative energy gradient method with interacting quantum atoms to determine the reaction mechanism and catalytic effects in the peptide hydrolysis in HIV-1 protease. *Chem. - Eur. J.* **2018**, *24*, 11200.

(39) Popelier, P. L. A.; Maxwell, P. I.; Thacker, J. C. R.; Alkorta, I. A relative energy gradient (REG) study of the planar and perpendicular torsional energy barriers in biphenyl. *Theor. Chem. Acc.* **2019**, *138*, 12.

(40) Thacker, J. C. R.; Popelier, P. L. A. The ANANKE relative energy gradient (REG) method to automate IQA analysis over configurational change. *Theor. Chem. Acc.* **2017**, *136*, 86.